

## End wall effects on the transitions between Taylor vortices and spiral vortices

S. Altmeyer,<sup>1</sup> Ch. Hoffmann,<sup>1</sup> M. Heise,<sup>2</sup> J. Abshagen,<sup>2</sup> A. Pinter,<sup>1</sup> M. Lücke,<sup>1</sup> and G. Pfister<sup>2</sup>

<sup>1</sup>*Institut für Theoretische Physik, Universität des Saarlandes, D-66123 Saarbrücken, Germany*

<sup>2</sup>*Institut für Experimentelle und Angewandte Physik, Universität Kiel, D-24098 Kiel, Germany*

(Received 7 August 2009; revised manuscript received 6 May 2010; published 23 June 2010)

We present numerical simulations as well as experimental results concerning transitions between Taylor vortices and spiral vortices in the Taylor-Couette system with rigid, nonrotating lids at the cylinder ends. These transitions are performed by wavy structures appearing via a secondary bifurcation out of Taylor vortices and spirals, respectively. In the presence of these axial end walls, *pure* spiral solutions do not occur as for axially periodic boundary conditions but are substituted by primary bifurcating, stable wavy spiral structures. Similarly to the periodic system, we found a transition from Taylor vortices to wavy spirals mediated by so-called wavy Taylor vortices and, on the other hand, a transition from wavy spirals to Taylor vortices triggered by a propagating defect. We furthermore observed and investigated the primary bifurcation of wavy spirals out of the basic circular Couette flow with Ekman vortices at the cylinder ends.

DOI: [10.1103/PhysRevE.81.066313](https://doi.org/10.1103/PhysRevE.81.066313)

PACS number(s): 47.20.Ky, 47.32.cf, 47.54.-r

### I. INTRODUCTION

One of the classical systems for the study of bifurcations and nonlinear pattern formation is the Taylor-Couette system, i.e., the flow of a viscous fluid in the annular gap between two concentric and independently rotating cylinders [1,2]. It is one of the best controllable hydrodynamic systems and allows quantitative comparisons between experiments and numerical simulations of the Navier-Stokes equations also beyond the first instabilities. Under the assumption of an axially infinite system, the basic flow state is the rotationally symmetric, axially homogeneous circular Couette flow (CCF) [3].

It undergoes—depending on the inner and outer cylinder rotation rates  $\Omega_{1,2}$ —a large variety of symmetry breaking bifurcation scenarios. The axisymmetric, toroidally closed Taylor vortex flow (TVF) and the helical, open spiral vortices (SPI) which are symmetry degenerated into left-winding spirals and right winding spirals are the essential flow structures for the parameter values considered here [1,4]. The ribbon state (RIB) can be seen as a nonlinear superposition of the two oppositely propagating spirals [2,5,6]. Several theoretical and experimental investigations concern the interaction between TVF, SPI, and a variety of different wavy solutions [7–16]. Figure 1 gives a schematic overview of the structures discussed in this paper in the  $\varphi$ - $z$ -plane of an unrolled cylinder surface.

TVF (SPI) appears via a primary pitchfork (Hopf) bifurcation out of CCF [2]. Their stability at onset is regulated by the order of the appearance upon increasing  $\Omega_1$ : the first solution to bifurcate out of CCF is stable and the second one is unstable. However, the second unstable solution can become stable at higher  $\Omega_1$ . Which state bifurcates first depends among others on  $\Omega_2$  [1,2]. The ribbon solution is unstable within the whole parameter range investigated here. Besides parameter regions with monostability of TVF or of SPI, one also observes regions with bistability of both states [17]. When moving the control parameters out of such a region, one solution loses its stability and the flow undergoes a transition to the remaining stable state, i.e., from TVF to SPI or vice versa.

The stability is transferred from TVF to SPI via secondarily bifurcating wavy Taylor vortices (wTVF) [9,10] and from SPI to TVF via secondarily bifurcating wavy spiral vortices (wSPI) [18]. This is shown by bifurcation theoretical considerations and symmetry arguments [7,8] as well as by amplitude expansion techniques [9] and numerical simulations [18] for the axially periodic case (pbc). For this setup, we presented in [18] how the solution branches of TVF and SPI are connected via the unstable ribbon state and intermediate stable wavy solutions.

We use the acronyms wTVF and wSPI to describe states in which Taylor vortices and spiral vortices are azimuthally modulated but remain toroidally closed into themselves or helical, respectively (c.f. Fig. 1). The wTVF state was known to appear via a secondary forward bifurcation out of TVF [9,10] and the wTVF solution branch has been seen to return to the TVF branch or to undergo higher order bifurcations [10–13,19,20] at larger driving.

In finite systems where the fluid is confined by axial end walls, e.g., nonrotating lids, the axial translation invariance is broken. These end walls generate at any driving rate disturbances in the form of axisymmetric vortices with an amplitude that is decaying roughly exponentially into the bulk. For small rotation frequencies of the inner cylinder these so called Ekman vortices overlay and deform the CCF to a new

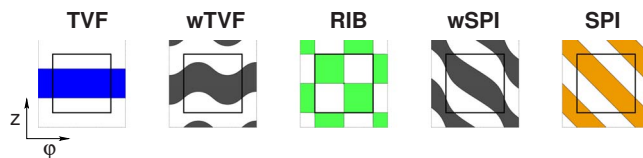


FIG. 1. (Color online) Schematic illustrations of the vortex structures discussed in this paper. The colored (gray shaded) regions denote radial outflow,  $u > 0$ , and the white ones indicate radial inflow,  $u < 0$ , respectively, in the plane of an unrolled cylinder surface in the annulus. The inner squares cover the azimuthal period  $2\pi$  in horizontal direction and one axial wavelength  $\lambda$  in vertical direction. For better visibility the structures are periodically continued slightly beyond these limits. The wSPI and SPI with azimuthal wave number  $M=1$  are shown in their left-winding variety.

stationary, rotationally symmetric basic flow and show Ekman induced intensity variations.

Here we identify this flow in finite systems with a side-wall induced Ekman vortex structure adjacent to the lids and CCF-like behavior in the bulk with words (also in combination) like basic, CCF-Ekman, or only Ekman, depending on the context. The rotationally symmetric Ekman mode always contributes to the axial Fourier spectra of other flow states and it significantly influences their structure, bifurcation behavior, stability, and dynamics. This has been the subject of many publications [1,14–16,21–24].

Spirals, for instance, propagate in finite systems between a phase generating and a phase annihilating Ekman-spiral defect. Such defects separate the bulk that is filled with spiral vortices from the Ekman vortices in the vicinity of both end walls [25,26]. Here, the axial wave number of the spirals in the bulk is almost independent of the aspect ratio. On the other hand, the distance between the end walls crucially influences the axial wave number of TVF [25]. Furthermore, rigid boundary conditions (rbc) [3] lead to solutions which contain large *axisymmetric* mode components.

In Sec. II we describe the system and our methods of investigation. In Sec. III we briefly review the bifurcation behavior under axially periodic boundary conditions. This review sets the stage for presenting our main results in Sec. IV. Therein we elucidate how TVF transforms into wSPI and vice versa in the presence of nonrotating rigid lids at the cylinder ends. We focus on bifurcation properties, stability, and spatiotemporal dynamics of the involved flow states. In the first part of Sec. IV the transition from TVF to wSPI via wTVF is discussed. The second part deals with the transition from wSPI to TVF via a propagating defect. In each case frequencies and wave number selection are discussed. Furthermore, comparisons of rbc results are made with pbc results as well as with experimental data.

## II. SYSTEM

In our Taylor-Couette system a Newtonian fluid of kinematic viscosity  $\nu$  fills the annular gap between two concentric, independently rotating cylinders (inner, outer radius  $r_{1,2}$ ; angular velocities  $\Omega_{1,2}$ ). We consider a fixed radius ratio of  $\eta=r_1/r_2=0.5$  and a fixed length  $\Gamma=12$  in units of the gap width  $d=r_2-r_1$ . Nonrotating, rigid lids close the gap and serve as axial end walls. In Fig. 2 that shows the geometry of the Taylor-Couette system the bottom lid is indicated schematically as well.

Cylindrical coordinates  $r, \varphi, z$  are used to decompose the velocity field into a radial component  $u$ , an azimuthal one  $v$ , and an axial one  $w$

$$\mathbf{u} = u\mathbf{e}_r + v\mathbf{e}_\varphi + w\mathbf{e}_z. \quad (1)$$

The system is governed by the Navier-Stokes equations

$$\partial_t \mathbf{u} = \nabla^2 \mathbf{u} - (\mathbf{u} \cdot \nabla) \mathbf{u} - \nabla p. \quad (2)$$

Here, lengths are scaled by the gap width  $d$ , times by the radial diffusion time  $d^2/\nu$  for momentum across the gap, and the pressure  $p$  by  $\rho\nu^2/d^2$ . The Reynolds numbers

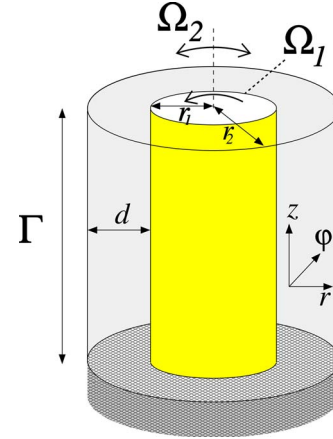


FIG. 2. (Color online) Geometry of the Taylor-Couette system. Only the bottom lid serving as one of the axial end walls is indicated (dark gray).

$$R_1 = r_1 \Omega_1 d / \nu, \quad R_2 = r_2 \Omega_2 d / \nu \quad (3)$$

enter into the boundary conditions for  $v$ :  $R_1$  and  $R_2$  are just the reduced azimuthal velocities of the fluid at the cylinder surfaces. Within this paper, we hold the outer Reynolds number fixed at  $R_2 = -100$ .

For numerical simulations, we used the G1D3 code that is described in [4,17]. It is a combination of a finite differences method in time and in radial and axial direction and a Galerkin expansion in  $\varphi$  direction with a decomposition

$$f(r, \varphi, z, t) = \sum_m f_m(r, z, t) e^{im\varphi} \quad (4)$$

of all fields  $f \in \{u, v, w, p\}$ .

In the experimental setup, the inner cylinder of radius  $r_1 = (12.50 \pm 0.01)$  mm is machined from stainless steel. The outer cylinder of radius  $r_2 = (25.00 \pm 0.01)$  mm is made from optically polished glass. As fluid thermostatically controlled silicone oil with a kinematic viscosity  $\nu = 10.6$  cS is used. The tilt of the massive, nonrotating end walls confining the fluid at bottom and top is better than 0.03 mm at the outer diameter. The flow is visualized by elliptical aluminum particles having a length of 80  $\mu\text{m}$ . Flow visualization measurements are performed by monitoring the system with a charge-coupled device (CCD) camera in front of the cylinder. It records the luminosity along a narrow axial stripe. The spatiotemporal behavior of the flow is then represented by successive stripes for each time step at a constant  $\varphi$ -position leading to continuous space-time plots.

## III. TRANSITIONS IN AXIALLY PERIODIC SYSTEMS

Before we present in the next section the results for the transition behavior and the spatiotemporal properties of vortex flows in finite-length systems subject to rigid boundary conditions that are axially imposed by rigid nonrotating lids at both cylinder ends we review here shortly the pbc case of axially periodic boundary conditions.

In [18] the transitions from TVF to SPI and vice versa were elucidated for this idealized case. Therein the solution

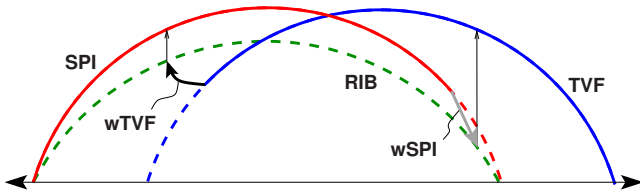


FIG. 3. (Color online) Schematic bifurcation diagram of vortex flow amplitudes versus control parameter, e.g.,  $R_2$  along the horizontal axis. Stable (unstable) solutions subject to axially periodic boundary conditions are displayed as solid (dashed) lines. TVF, SPI, and RIB (ribbon state) denote nonhysteretic solution branches that bifurcate out of the CCF state. The solutions for wTVF and wSPI are indicated by thick arrows. Thin arrows indicate the transients corresponding to the “jump” bifurcation mentioned in [7].

branch of stable TVF is connected to the unstable ribbon branch via stable wTVF. And the branch of stable SPI connects to the ribbon solution via wSPI. Then, a ‘jump’ bifurcation [7] from the end of the stable wTVF (wSPI) leads to the stable SPI (TVF) branch.

This bifurcation behavior is schematically illustrated in Fig. 3. It reflects the facts that in solution space (i) the parameter region of stable wTVF (wSPI) separates the region of bistable SPI and TVF from the regions with monostable SPI (TVF) and, furthermore, that (ii) the stable wTVF (wSPI) coexist bistably with SPI (TVF) in the respective regions.

Each of these structures is characterized by a small set of significant Fourier modes,  $e^{i(m\varphi+kz)}$ , that we denote in the following by the abbreviation  $(m,k)$ . These modes reflect and determine the symmetry properties of the vortex structures. Thus, e.g., the Fourier spectrum of the TVF solution contains a dominant  $(0,k)$  mode and its complex conjugate  $(0,-k)$ . The spectrum of left handed SPI with azimuthal wave number  $M=1$  is dominated by  $(1,k)$  and its complex conjugate  $(-1,-k)$ . Its mirror image, the right handed SPI contains  $(1,-k)$  and  $(-1,k)$  as dominant contributions. In the following we do no longer mention the complex conjugates separately.

All these modes  $[(0,k),(1,k),(1,-k)]$  contribute to the wavy solutions: wTVF have a dominant  $(0,k)$  and in addition an admixture of the two spiral modes  $(1,\pm k)$  with equal amplitude. The wSPI spectrum contains both spiral modes, a dominant  $(1,k)$  and a weaker  $(1,-k)$  mode or vice versa and additionally, a small contribution of the  $(0,k)$  mode.

Nonrotating rigid lids at the axial ends of the annular gap lead to an important difference in comparison to the above described situation under pbc: *pure* SPI solutions in the strict sense do no longer exist. They are replaced by wSPI that are modified by the presence of a  $m=0$  contribution from the Ekman mode. These wSPI appear under rbc via a primary bifurcation out of the basic CCF-Ekman flow and they play a similar role as the SPI under pbc. Furthermore, wSPI loose under rbc their stability for higher  $R_1$  and we found traveling defects which trigger a transition from wSPI to stable TVF.

#### IV. TRANSITIONS IN FINITE-LENGTH SYSTEMS

This section describes in the first part the bifurcation from TVF to wSPI via wTVF and in the second part the transition

from wSPI to TVF in an annulus of finite length with nonrotating lids. As in the periodic system [18], we also found here transitions between the two primary bifurcating structures, namely TVF and wSPI in this case. The main difference between both is that we do not observe (neither in simulations nor in experiments) *pure* spirals for  $\Gamma=12$  systems. In a *pure* SPI state the flow is periodic in  $\varphi, z$ , and  $t$ , say, with axial wave number  $k$ , azimuthal wave number  $M$ , and frequency  $\omega$ . Furthermore, the helical flow does not depend on  $\varphi, z, t$  separately but only on the combined phase variable  $\phi=M\varphi+kz-\omega t$  so that any field displays the continuous symmetry  $f(r, \varphi, z, t)=f(r, \phi)$  (c.f. [27]).

In finite systems with Ekman vortices near the nonrotating end walls pure SPI are replaced by wSPI. The latter have a more complex mode spectrum as described in [18]. This is due to the interaction between the spiral modes and the rotationally symmetric Ekman modes. We finally mention that in the absence of symmetry breaking axial through-flow right-handed and left-handed SPI are equivalent to each other [17,25] and that holds also for wSPI in the rbc case. We thus distinguish between the different helicities in this paper only when needed.

In Fig. 4(a), we compare the bifurcation behavior of TVF, SPI, wTVF, and wSPI subject to rbc with the one for pbc in Fig. 4(b). The comparison is done by first of all identifying in the rbc case the local axial wave number  $k$  of the investigated pattern in the bulk at midheight,  $z \approx \Gamma/2$ . We present here in Fig. 4(a) results for TVF, wTVF, and SPI with  $k=4.85$  and in addition also for SPI and wSPI with  $k=3.95$ . The results in the pbc case for the corresponding patterns with these two wave numbers are shown in Fig. 4(b).

The comparison is based on using the azimuthal decomposition [Eq. (4)] of the radial velocity field. In it we performed an axial Fourier analysis of the mode amplitudes  $u_m(z, t)$  at midgap,  $r=r_1+d/2$ . We then identified for  $m=0$  and  $m=1$  the largest contribution in the axial Fourier spectrum of  $u_m(z, t)$  for the patterns with  $k=4.85$  and  $k=3.95$ .

The moduli of these dominant Fourier amplitudes are denoted by  $|u_{m,k}|$  and plotted in Fig. 4(a) for the rbc case and in Fig. 4(b) for the pbc case, respectively. Figures 4(c) and 4(d) show the frequencies  $|\omega_{m,k}|$  with which the corresponding complex Fourier amplitudes oscillate. The different vortex structures are distinguished by lines with symbols as explained in the legend of Fig. 4(a). Solid (dashed) lines with filled (open) symbols represent stable (unstable) solutions.

The unstable TVF branches in (a,b) have been obtained in the rbc case and the pbc situation by imposing rotational symmetry in the calculations. The unstable ribbons in (b,d) were determined for pbc only with our G2D2 code. It uses Fourier expansions not only in azimuthal but also in axial direction. This allows to restrict the modes such that the ribbon solution branch gets stabilized [18].

#### A. Transition from TVF to wSPI

We start our discussion of the bifurcation diagram in Fig. 4(a) in region E' with a stable  $k=4.85$  TVF state. Upon reducing  $R_1$ , it loses its stability at the border between E' and F' and remains unstable thereafter. This behavior is the same

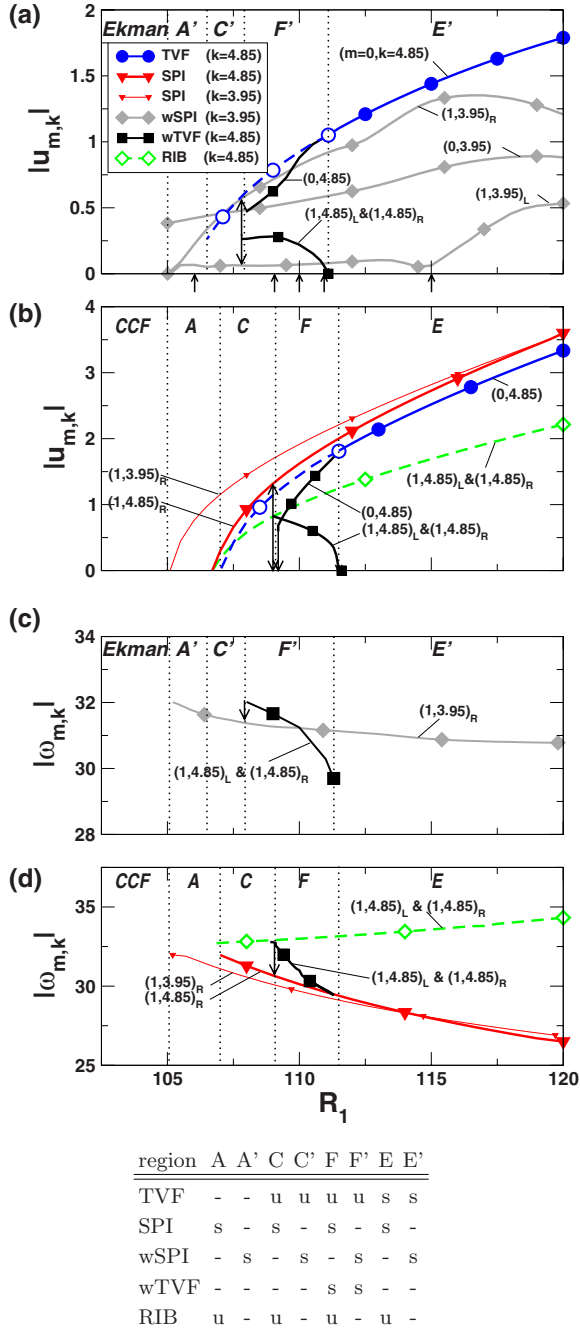


FIG. 4. (Color online) Numerically obtained bifurcation diagrams of TVF, SPI, wTVF, wSPI, and ribbons (RIB) versus  $R_1$  for rbc (a,c) and for pbc (b,d). The axial wave numbers  $k$  of these structures are indicated in the legend of (a). Solid (dashed) lines with filled (open) symbols refer to stable (unstable) states. Shown are the moduli  $|u_{m,k}|$  of the dominant axial Fourier amplitudes of the azimuthal modes  $u_m(z,t)$  [Eq. (4)] of the radial flow at midgap and the corresponding frequencies  $|\omega_{m,k}|$ ; see text for further explanations. The indices R and L correspond to right- and left-handed spiral modes. The short arrows below the abscissa of (a) denote  $R_1$ -values of snapshots in Fig. 5. The long arrows in the figures indicate transients to final stable states. The partitions of the  $R_1$ -interval labeled by unprimed and primed letters correspond to the stability regions for the pbc case [18] in (b,d) and the rbc case in (a,c), respectively. They are listed in table with s denoting stable, u unstable, and—nonexistent.

as under pbc (b). However there are some differences: (i) the stability thresholds are slightly different. (ii) The unstable TVF flow in (a) transforms into the CCF-Ekman state instead of ending in the CCF state as in (b). Moreover, when decreasing  $R_1$  in (a) into region A' and further below, the local wave number in the bulk of the unstable TVF state changes at the border between C' and A' from  $k=4.85$  to  $k=3.95$  in the CCF-Ekman state. For reasons of visibility we do not display the small amplitude  $|u_{0,k=3.95}|$  of the unstable, rotationally symmetric vortex flow solution in A' and in the leftmost region of Fig. 4(a). But the most important difference is (iii) that in C' and A' there exists a stable wSPI and not a pure SPI as in C and A. A detailed description of the stability properties, the bifurcation behavior, and the spatiotemporal structure of wTVF and wSPI is given, e.g., in [18].

In F' and F, TVF is unstable against wTVF which maintains the same wave number,  $k=4.85$ . Note, however, that the wave number in (b) is fixed by the predefined periodicity length of pbc. At the right border of C wTVF undergoes a transition to the remaining stable SPI solution with  $k=4.85$ . But in the rbc case wTVF transforms at the right border of C' to a stable wSPI solution with a different wave number, namely,  $k=3.95$ .

We added in (b) also the  $k=3.95$  SPI solution branch in order to document that the  $k=3.95$  SPI in the pbc case (b) has the same onset as the  $k=3.95$  wSPI in the rbc case of (a). Note also that the pbc SPI solution in (b) and the rbc wSPI solution in (a) are stable in the whole parameter range displayed here.

The transition from the unstable wTVF in (b) along the vertical arrows to SPI involves an unstable ribbon state appearing transiently. On the other hand, in the transition from wTVF to wSPI along the arrows in (a), i.e., in the rbc case, we did not find evidence for a transient ribbon state: The (0, 4, 85) mode (which appears in wTVF but not in ribbon states) does not vanish and not even diminishes with our ramping protocol during the transition wTVF  $\rightarrow$  wSPI at the border between C' and F' as it should for (transient) ribbons. We have omitted the (0, 4, 85) mode in C' because in the spectrum of the  $k=3.95$  wSPI, it is negligible compared to the three significant  $k=3.95$  modes.

Generally speaking, there are three major aspects of comparing the finite-length system in Fig. 4(a) with the periodic one in Fig. 4(b): (i) wSPI in (a) play quite the same role as the pure SPI in (b)—we indicated this also by the primed letters A', C', E', and F' that label the stability regions in the rbc case in analogy to the pbc situation [18,25] with unprimed letters. (ii) During the transition from TVF via wTVF to wSPI, the finite  $\Gamma=12$  system selects for the parameters of Fig. 4 the wave number  $k=4.85$  for TVF and wTVF but a different one for wSPI, namely,  $k=3.95$ . Thus, the transition between the toroidally closed TVF and wTVF structures preserves the wave number whereas it is changed during the transient to the helical wSPI structure. (iii) The axial end walls in the rbc case generate rotational symmetric Ekman flow that modifies all vortex structures discussed here. As a consequence, all thresholds [dotted vertical lines in Figs. 4(a) and 4(b)] for the appearance or change of rotational and toroidal flows in the bulk are shifted toward lower  $R_1$  com-

pared to the respective thresholds in the periodic system. But the onsets for wTVF in both cases, i.e., the lines between E, F, and E', F', respectively, coincide quite well.

**1. Frequencies**

Figures 4(c) and 4(d) provide frequencies  $|\omega_{m,k}|$  with which the relevant complex mode amplitudes in (a) and (b) oscillate. The rotationally symmetric modes  $(0,k)$  contributing to axially nonpropagating TVF and wTVF patterns are real and do not oscillate. Since wTVF is a time-periodic rotating state that does not propagate axially, all mode frequencies are either zero ( $\omega_{0,4.85}=0$ ) or multiples of  $\omega_{1,4.85}$ . So, the dynamics of wTVF is rather simple while the spatial structure is more complex

Spirals and ribbons grow for pbc (d) via a primary Hopf bifurcation with a common frequency out of CCF and then develop differently with increasing  $R_1$ . The difference between the spiral frequencies for pbc (d) and rbc (c) is a consequence of the Reynolds-stress driven, intrinsic axial net flow which is directed under pbc oppositely to the spiral propagation. In finite systems, this net flow is suppressed by the rigid end walls which leads to a shift in the axial phase velocity and thereby also in the frequency [17]. This effect can be seen by comparing the wSPI frequencies in (c) with the SPI frequencies in (d). Note finally that the SPI frequencies for pbc with  $k=3.95$  and  $k=4.85$  are nearly identical.

On the other hand, the wTVF frequencies are much less influenced by the different boundary conditions. In fact, at the bifurcation thresholds E-F and E'-F' they are almost identical. The reason is that here, the intrinsic net flow of the left-handed  $(1,4.85)_L$  mode is compensated by that of the  $(1,4.85)_R$  mode contributing with equal amount to the wTVF state. This holds for the pbc as well as for the rbc situation. Moreover, the variation of wTVF and of (w)SPI frequencies in region F (F') differs significantly.

Finally we should like to comment on the fact that under pbc the frequency of wTVF at its onset at the right border of region F in Fig. 4(d) is very close to the nonlinear SPI frequency there. This was observed previously in [18]. But it was not known whether this agreement between the rotation frequency of the wTVF's modulation and the rotation frequency of the SPI had a deeper spatiotemporal reason. Now we found the rbc frequency of wTVF at its onset at the right border of region F' in Fig. 4(c) to differ significantly from that of the wSPI there. Thus, we tend to conclude that the above described similarity between the two frequencies under pbc is accidental.

**2. Spatiotemporal behavior**

To display the spatiotemporal evolution of the flow in the transitions between the various vortex structures discussed here we apply two different methods: from our numerical results we construct three-dimensional (3D) plots of isosurfaces of the azimuthal vorticity  $\partial_z u - \partial_r w$ . In addition and as a complimentary information we show experimental flow visualization—as described at the end of Sec. II—for the numerically documented transitions.

Figure 5(a) shows how the isosurfaces of the azimuthal vorticity change in the transition TVF (snapshot No. 5)

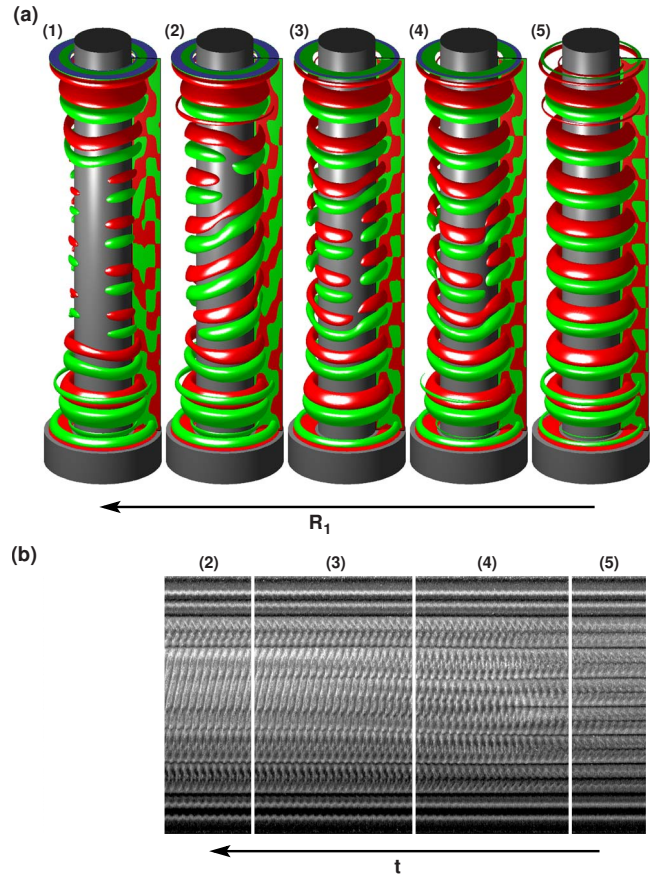


FIG. 5. (Color online) Spatiotemporal changes of the vortex structure in the transition TVF  $\rightarrow$  wTVF  $\rightarrow$  wSPI (from right to left). (a) Numerically obtained snapshots of isosurfaces of the azimuthal vorticity  $\partial_z u - \partial_r w = \pm 40$  [red (dark gray): +40, green (light gray): -40]. The whole  $2\pi$ -cylinder is displayed to present the whole structure in one single 3D plot. In the  $r-z$ -plane shown at the right side of each cylinder for a fixed  $\varphi$ , red (dark gray) implies positive vorticity and green (light gray) negative vorticity. The Reynolds numbers for the snapshots [ $R_1=106$  (No. 1), 109 (No. 2), 110 (No. 3), 111 (No. 4), 115 (No. 5)] are marked by arrows below the abscissa of Fig. 4(a). All snapshots in (a) represent “stationary” (i.e., fully relaxed, nontransient) structures. (b) Experimental flow visualization after an instantaneous jump from  $R_1=115$  down to 109. The space-time plots result from successively recording the luminosity at a fixed  $\varphi$ -position along a narrow axial stripe with a CCD-camera in front of the cylinder. The shown records cover about 13 diffusion times after the jump. All plots in (a) and (b) cover the whole system length  $\Gamma=12$ .

$\rightarrow$  wTVF (No. 4, No. 3)  $\rightarrow$  wSPI (No. 2, No. 1). The isosurfaces in the snapshots of Fig. 5(a) belong to “stationary”—in the sense of fully relaxed, nontransient—states at  $R_1$  values that are marked by short arrows below the abscissa of Fig. 4(a).

With decreasing  $R_1$  the TVF state (No. 5) becomes unstable against toroidally closed, axially modulated wTVF (No. 4) keeping its axial wave number  $k=4.85$ . In the wTVF structure the modulation amplitude increases from both ends toward midheight where the Ekman influence is minimal. As the  $m \neq 0$  mode contributions grow with decreasing  $R_1$ , the formerly rotational symmetric TVF structure becomes more

and more deformed and the vorticity tubes narrow at a certain  $\varphi$ -position (No. 4). This means that the maximal vorticity in the  $r$ - $z$  plane at this  $\varphi$ -position decreases with  $R_1$ —the vortex intensity becomes weaker there. Note that this indentation of the vortex tubes as well as the defect rotate with the whole structure as in a rigid-body rotation. Finally, the isosurfaces become completely constricted and separated (No. 3). After displacing the ends of the tubes, new connections are established and the vorticity increases now to the final distribution in the wSPI (No. 2) with the smaller wave number,  $k=3.95$ . The last snapshot, No. 1, depicts a situation with weakly supercritical wSPI of small azimuthal vorticity. Here the remaining strong Ekman vortices dominate the isotropic vorticity surface at our chosen levels of  $\pm 40$ .

Figure 5(b) presents the experimentally obtained spatiotemporal behavior of the flow after an instantaneous step in Reynolds number from  $R_1=115$  down to 109, c.f. caption for more details. The initial state in plot No. 5 is TVF with a wave number of  $k \approx 4.8$ . After the step down in  $R_1$  it undergoes in plot No. 4 a transition to wTVF that starts at mid-height with the same axial wave number. After a transient shown in plot No. 3 which corresponds to the ‘jump’ bifurcation described above, wSPI with  $k=3.95$  is finally established in plot No. 2.

In addition to the above described one-step protocol from  $R_1=115$  down to 109 we have also realized other step and ramp histories with various Reynolds numbers at their ends in order to check that the TVF (No. 5), wTVF (No. 4), and wSPI (No. 2) states are also in our experiments stationary and stable. Comparing the outcome of these different protocols we found that the intermediate flow states of wTVF and wSPI which occur in a transient manner after the step down from  $R_1=115$  all the way to  $R_1=109$  are topologically identical to the stationary counterparts that are stable at fixed  $R_1$  values in between. That means in No. 5, one can see in the experiments wavy spirals, in No. 4 the beginning of the modulation of the Taylor vortices, and finally in No. 2, one sees in the bulk of the system spiral flow delimited by Ekman vortex structures at the top and the bottom.

### 3. Wave number selection

Due to the finite boundary conditions, the toroidally closed structures (TVF, wTVF) can occur with discretely different axial wave numbers depending on the initial conditions. In the parameter region  $E'$  of Fig. 4 we found at least three stable TVF states. They had 7, 8, and 9 vortex pairs with local wave numbers at midheight  $k=3.83$ , 4.85, and 5.81, respectively. However, in Figs. 4 and 5 only the TVF state with 8 vortex pairs is presented. All these three TVF states undergo a transition to wTVF in region  $F'$  for specific  $R_1$  values without changing their respective wave number  $k$ . Finally, all wTVF states ‘‘jump’’ with a change in  $k$  to the  $k=3.95$  wSPI solution.

The wave numbers were measured at midgap near mid-height with an accuracy of about 3% in the numerical simulations and about 4% in experiments. The experimental

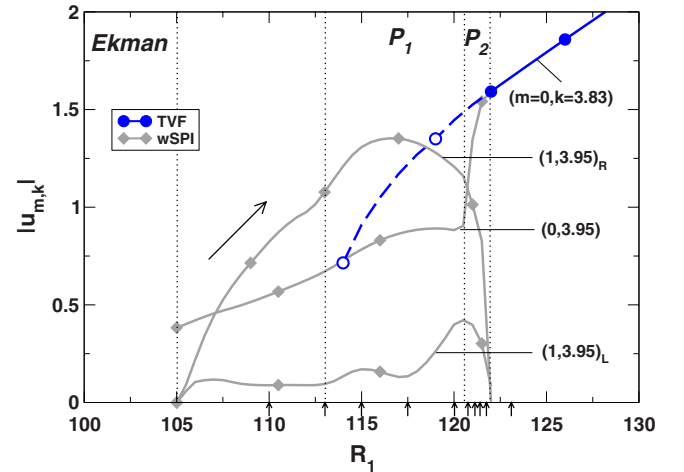


FIG. 6. (Color online) Numerically obtained bifurcation diagrams of TVF and wSPI versus  $R_1$  for rbc. See caption of Fig. 4(a) for an explanation of the details. The short arrows below the abscissa identify the  $R_1$ -values of the snapshots in Fig. 7(a). The long arrow indicates the direction of the transition wSPI  $\rightarrow$  TVF as discussed in Sec. IV B. Region  $P_2$  includes the behavior of the amplitudes during the transformation of wSPI into wTVF.

values,  $k=4.53$  for (w)TVF and  $k=4.03$  for wSPI, differ slightly from the numerical ones,  $k=4.85$  for (w)TVF and  $k=3.95$  for wSPI, respectively. However, numerical simulations as well as experimental results exhibit the same jumps in  $k$  during the transition wTVF  $\rightarrow$  wSPI.

## B. Transition from wSPI to TVF

Under pbc, one finds the bifurcation sequence SPI  $\rightarrow$  wSPI  $\rightarrow$  TVF. Here, the transition from wSPI to TVF is mediated by a ‘‘jump’’ bifurcation [7,18]. Under rbc, first of all, pure SPI do not exist as described above. Rather SPI are replaced by wSPI which appear for stronger counter-rotation as a stable solution via a primary bifurcation out of the basic CCF-Ekman flow.

In addition, we found that this rbc wSPI solution branch becomes unstable against TVF via another kind of transition that occurs beyond region  $E'$  of Fig. 4(a). This transition is mediated by a propagating defect which separates the wSPI from a wTVF regime pushing wSPI out and pulling wTVF through the bulk. Once the defect has traversed the whole bulk, the modulation amplitude of the wTVF vanishes and TVF remains as stable final state.

This rbc transition scenario from wSPI to TVF that is characterized by a propagating defect bears some resemblance with the one explored in Ref. [28]. There a defect which separates domains of oppositely traveling spiral waves propagates through the system and triggers a transition from right-handed to left-handed SPI or vice versa.

### 1. Bifurcation scenario

The bifurcation properties of the transition wSPI  $\rightarrow$  TVF are documented in detail in Fig. 6. This is a follow up of the bifurcation diagram in Fig. 4(a) with a slightly extended  $R_1$  range that focuses on the wSPI  $\rightarrow$  TVF transition. The short

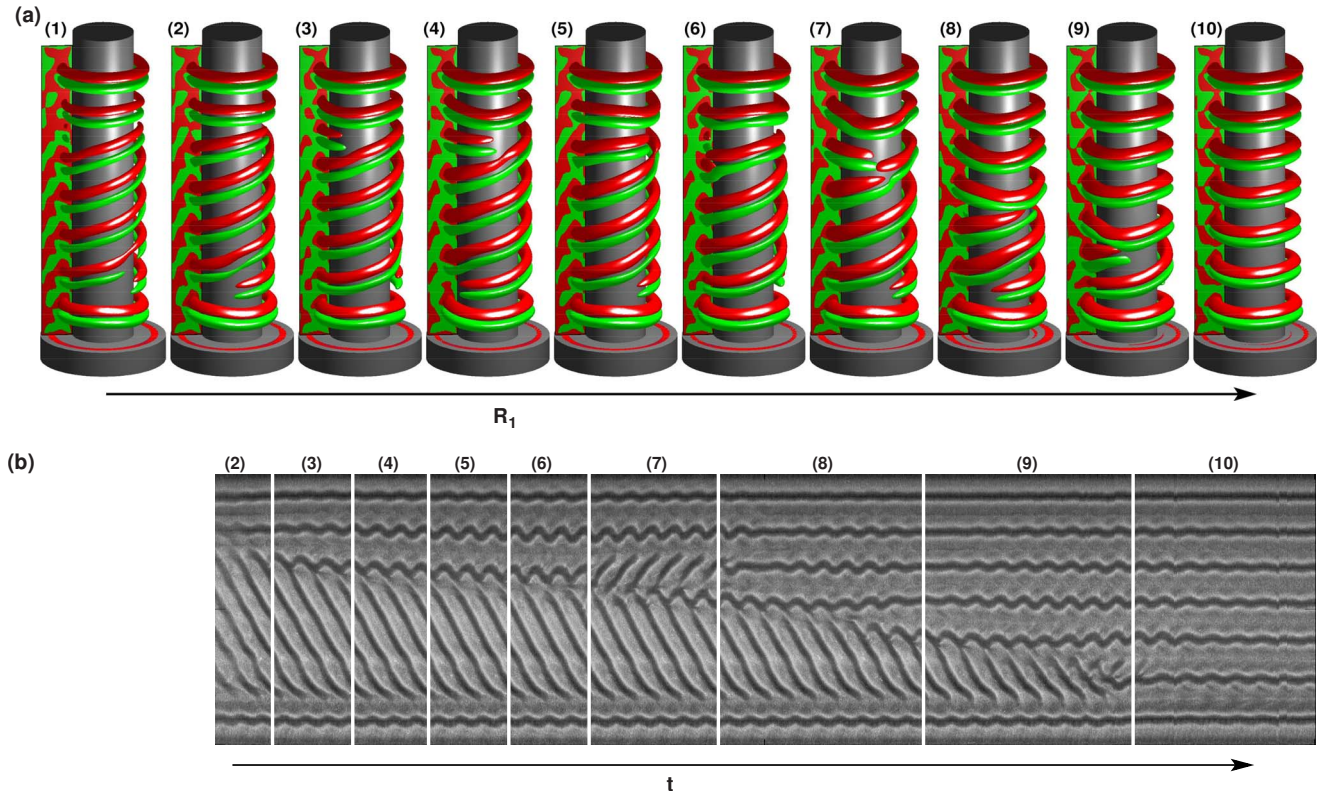


FIG. 7. (Color online) Spatiotemporal changes of the vortex structure in the transition wSPI→TVF (from left to right). (a) Numerically obtained snapshots of isosurfaces of the azimuthal vorticity  $\partial_z u - \partial_r w = \pm 40$  [red (dark gray): +40, green (light gray): -40]. The whole  $2\pi$ -cylinders is depicted to present the whole structure in one single 3D plot. In the  $r$ - $z$ -plane shown at the right side of each cylinder for a fixed  $\varphi$ , red (dark gray) implies positive vorticity and green (light gray) negative vorticity. The Reynolds numbers for the ten snapshots are marked by arrows below the abscissa of Fig. 6. The snapshots five to nine in (a) show transient flow structures with a downwards propagating defect that are described in more detail in the text. The other snapshots in (a) represent “stationary” (i.e., fully relaxed, nontransient) structures. (b) Experimental flow visualization after an instantaneous jump from  $R_1=107$  up to 120. The space-time plots result from successively recording the luminosity at a fixed  $\varphi$  position along a narrow axial stripe with a CCD camera in front of the cylinder. The shown records cover about 11 diffusion times after the jump. All plots in (a) and (b) cover the whole system length  $\Gamma=12$ .

arrows below the abscissa identify the  $R_1$  values for which isovorticity snapshots are presented in Fig. 7(a).

Let us start with a wSPI solution at small  $R_1$ . When increasing  $R_1$  beyond the left border of region  $P_1$  the Ekman-wSPI defect that separates the upper (modulated) Ekman structure from the wSPI becomes displaced further downward into the bulk. Thereby, a domain of wTVF opens up between the first Ekman vortices near the upper plate and the downward displaced wTVF-wSPI defect. However, for all  $R_1$  in the parameter region  $P_1$  of Fig. 6 this defect, while rotating azimuthally with the flow, remains at its axial position so that the axial extension of the wTVF region does not change.

Then, at the left border of  $P_2$ , this defect begins to propagate downward toward the other axial end. This is a transient flow which finally ends up in a pure  $k=3.83$  TVF solution after the annihilation of the propagating defect at the lower Ekman-spiral defect. The gray marked region  $P_2$  shows the behavior of the amplitudes during the transformation of wSPI into wTVF. We observed these transients within the range  $120 \leq R_1 \leq 122$  when we waited about 5 diffusion times between upward  $R_1$ -steps of size  $\Delta R_1 \approx 1$ . Upon decreasing the step size and increasing the waiting times between the  $R_1$ -steps substantially we expect that the gray

marked region  $P_2$  shrinks ideally to a line that separates the regimes of stationary and moving defect, respectively.

The final TVF state with  $k=3.83$  differs from the one discussed in Fig. 4(a) which has  $k=4.85$ . Both these TVF states are members of the family of stable TVF states with different wave numbers (c.f. Sec. IV A 3).

Note that the transition wSPI→TVF is symmetry degenerated: a right-winding wSPI like the one shown in the left part of Fig. 7 results in a downward propagating defect behind which the intermediate wTVF invades the wSPI region. A left-winding wSPI, on the other hand, is annihilated by an upward propagating defect that starts at the lower end of the cylinders and that expands the wTVF region from the bottom toward the top.

This numerically obtained transition sequence is corroborated by and compatible with experimental results that are presented in Fig. 7(b). There we show snapshots of the spatiotemporal flow visualization of the transients after an initial jump (at the left border of the plot) from  $R_1=107$  to 120. In this sequence, both, the aforementioned “stationary” wSPI states as well as the subsequent invasion of the wSPI region by wTVF behind a downward propagating defect or front, respectively, appear as transient flow structures.

**2. Spatiotemporal behavior and wave number selection**

In Fig. 7(a) we show ten snapshots of numerically obtained isosurfaces of the azimuthal vorticity taken at the  $R_1$ -values that are marked by the small arrows below the abscissa of Fig. 6. This together with the spatiotemporal plot of the experimentally obtained velocity field in Fig. 7(b) illustrates the structural changes during the transition  $wSPI \rightarrow TVF$ .

Starting with a  $wSPI$  state (No. 1) in Fig. 7 and increasing  $R_1$ , the second closed vortex pair from the top becomes wavylike deformed. Simultaneously the  $wTVF$ - $SPI$  defect between the upper closed but modulated vortices and  $wSPI$  extending into the bulk gets displaced further downward to a new axial location (Nos. 2–5). This wavy deformation and the defect rotate with the whole structure. The modulation amplitude of the deformation becomes stronger with increasing  $R_1$  until the defect begins to propagate downward (Nos. 6–9), thereby pushing the  $wSPI$  domain downward and pulling a  $wTVF$  state through the system. In this way the  $wSPI$  domain shrinks and the  $wTVF$  domain grows.

During this process, neither the wave number of  $wSPI$  nor that of  $wTVF$  change significantly, because new  $wTVF$  vortices are generated directly behind the propagating defect: Comparing (No. 7) and (No. 8), one observes that the vortex tubes become constricted and separated and after displacing the ends of the tubes, new connections are established and a new  $wTVF$  vortex is generated. Finally, the defect reaches the bottom end and merges with the lower Ekman vortex (No. 10) leaving behind a pure TVF state.

Figure 7(b) experimentally elucidates the spatiotemporal behavior during the transition after an initial jump from  $R_1 = 107$  to 120 at the left border of the plot. As in the numerical simulations, the experimental step protocol realizes a transition from  $wSPI$  to TVF via a propagating defect. The experimentally obtained spatiotemporal plots in Fig. 7(b) after the sudden increase in  $R_1$  show a sequence of transient structures which roughly correspond to stationary structures in Fig. 7(a) that we see in our simulations with small stepwise, quasi-static changes of  $R_1$ . Furthermore, the experimental wave numbers for  $wSPI$   $k=4.03$  and TVF  $k=3.84$  agree very well with the numerical wave numbers for  $wSPI$   $k=3.95$  and TVF  $k=3.83$ .

**V. SUMMARY**

We have investigated the bifurcation behavior for the transition between Taylor vortices and wavy spirals in a finite-length Taylor-Couette system with nonrotating, rigid lids. In contrast to periodic boundary conditions where pure SPI solutions exist (even for outer cylinder at rest), here, helical solutions occur as  $wSPI$  due to the admixture of Ekman induced  $m=0$  mode components in the Fourier spectra.

In the finite system geometry, we found a transition from TVF to  $wSPI$  via  $wTVF$  (schematically plotted in Fig. 8)

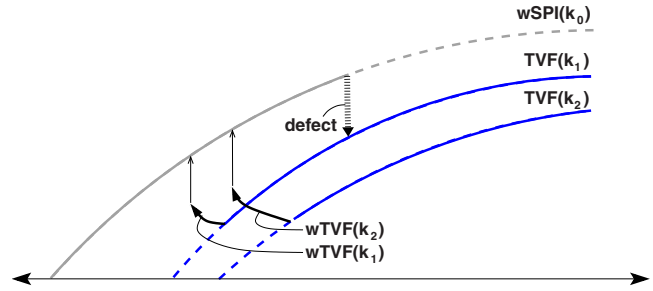


FIG. 8. (Color online) Schematic bifurcation diagram of flow amplitudes. It summarizes results for the finite system shown in Figs. 4(a) and 6. Stable (unstable) solutions are displayed as solid (dashed) lines. TVF solution branches are shown exemplarily for two possible wave numbers,  $k_1$  and  $k_2$ . In the transitions from TVF to  $wTVF$  they are preserved. Eventually  $wTVF$  (lines labeled  $wTVF$ ) undergo complex transients (thin vertical arrows) to  $wSPI$  with a uniquely selected wave number, say,  $k_0$ . The broad dashed arrow refers to the transition from  $wSPI$  to TVF that involves among others a propagating defect (see text for more details). Thereby, the TVF wave number closest to  $k_0$ , here  $k_1$ , is selected.

which is analogous to the transition from TVF to SPI via  $wTVF$  in the periodic system. The  $wSPI$  structure with helical open vortices selects a unique wave number. On the other hand, several bifurcation branches of TVF and  $wTVF$  states with toroidally closed vortices exist simultaneously and multistably with different axial wave numbers. The transitions between the toroidally closed structures of TVF and  $wTVF$  preserve the wave number, whereas the transitions between toroidally closed and helical structures are in general accompanied by a change in  $k$ .

The transition from SPI to TVF via  $wSPI$  that was found at moderate  $R_2$  for pbc differs from that one in the finite system due to the absence of a pure stable SPI solution. Instead, the finite system undergoes at stronger counter rotation rates a transition from  $wSPI$  to TVF which is triggered by an axially propagating defect (c.f. Fig. 8). This defect pushes the  $wSPI$  out of the system and pulls  $wTVF$  into the bulk that finally transforms into TVF. Thus, all in all the spatiotemporal complexity of the transition to TVF is larger in the rbc than in the pbc case.

A significant influence of rigid axial ends is the inhibition of any intrinsic, Reynolds stress driven through flow in SPI and  $wSPI$ . This leads to a difference in the (w)SPI frequencies for pbc and rbc. On the other hand, the  $wTVF$  frequencies in the pbc and rbc case are practically identical since the  $wTVF$  state does not support a net intrinsic through flow.

**ACKNOWLEDGMENTS**

We acknowledge support from the Deutsche Forschungsgemeinschaft.

- [1] R. Tagg, *Nonlinear Sci. Today* **4** (3), 1 (1994).
- [2] P. Chossat and G. Iooss, *The Couette-Taylor Problem* (Springer, New York, 1994).
- [3] Throughout this paper we use the abbreviations CCF: circular Couette flow TVF: Taylor vortex flow; SPI: spiral vortex flow; RIB: ribbons; wTVF: wavy Taylor vortex flow; wSPI: wavy spiral vortex flow; pbc: axially periodic boundary conditions; rbc: rigid boundary conditions corresponding to nonrotating axial end walls.
- [4] Ch. Hoffmann and M. Lücke, in *Physics of Rotating Fluids, Lecture Notes in Physics 459*, edited by C. Egbers and G. Pfister (Springer, Berlin, 2000), p. 55.
- [5] Y. Demay and G. Iooss, *J. Mec. Theor. Appl.*, special supplement 193 (1984).
- [6] A. Pinter, M. Lücke, and C. Hoffmann, *Phys. Rev. E* **76** 015301 (2007); **78** 015304(R) (2008); **78** 017303 (2008).
- [7] M. Golubitsky, I. Stewart, and D. Schaeffer, *Singularities and Groups in Bifurcation Theory II* (Springer, New York, 1988).
- [8] M. Golubitsky and W. F. Langford, *Physica D* **32**, 362 (1988).
- [9] G. Iooss, *J. Fluid Mech.* **173**, 273 (1986).
- [10] C. A. Jones, *J. Fluid Mech.* **157**, 135 (1985).
- [11] C. D. Andereck, S. S. Liu, and H. L. Swinney, *J. Fluid Mech.* **164**, 155 (1986).
- [12] J. Antonijoan and J. Sanchez, *Phys. Fluids* **12**, 3147 (2000).
- [13] J. Antonijoan and J. Sanchez, *Phys. Fluids* **14**, 1661 (2002).
- [14] A. Lorenzen, G. Pfister, and T. Mullin, *Phys. Fluids* **26**, 10 (1983).
- [15] W. S. Edwards, S. R. Beane, and S. Varma, *Phys. Fluids A* **3**, 1510 (1991).
- [16] O. Czarny, E. Serre, P. Bontoux, and R. M. Lueptow, *Theor. Comput. Fluid Dyn.* **16**, 5 (2002).
- [17] Ch. Hoffmann, M. Lücke, and A. Pinter, *Phys. Rev. E* **69**, 056309 (2004).
- [18] Ch. Hoffmann, S. Altmeyer, A. Pinter, and M. Lücke, *New J. Phys.* **11**, 053002 (2009).
- [19] G. Ahlers, D. S. Cannell, and M. A. Dominguez-Lerma, *Phys. Rev. A* **27**, 1225 (1983).
- [20] K. Park, *Phys. Rev. A* **29**, 3458 (1984).
- [21] M. A. Dominguez-Lerma, D. S. Cannell, and G. Ahlers, *Phys. Rev. A* **34**, 4956 (1986).
- [22] J. M. Lopez, F. Marquez, and J. Shen, *Fluid Dyn. Res.* **27**, 91 (2000).
- [23] T. B. Benjamin, *Proc. R. Soc. London, Ser. A* **359**, 1 (1978).
- [24] T. B. Benjamin, *Proc. R. Soc. London, Ser. A* **359**, 27 (1978).
- [25] Ch. Hoffmann, M. Lücke, and A. Pinter, *Phys. Rev. E* **72**, 056311 (2005).
- [26] J. Abshagen, M. Heise, J. Langenberg, and G. Pfister, *Phys. Rev. E* **75**, 016309 (2007).
- [27] A. Pinter, M. Lücke, and Ch. Hoffmann, *Phys. Rev. Lett.* **96**, 044506 (2006).
- [28] M. Heise, Ch. Hoffmann, J. Abshagen, A. Pinter, G. Pfister, and M. Lücke, *Phys. Rev. Lett.* **100**, 064501 (2008).